

Reversible Efficient Diffusion for Image Fusion

Xingxin Xu¹, Bing Cao², DongDong Li⁵, Qinghua Hu², Pengfei Zhu^{2,3,4}

¹School of New Media and Communication, Tianjin University

² School of Artificial Intelligence, Tianjin University

³ Low-Altitude Intelligence Laboratory, Xiong'an National Innovation Center

⁴ Xiong'an Guochuang Lantian Technology Co., Ltd.

⁵ National University of Defense Technology

{xuxingxin, caobing, huqinghua, zhupengfei}@tju.edu.cn, lidongdong12@nudt.edu.cn

Abstract

Multi-modal image fusion aims to consolidate complementary information from diverse source images into a unified representation. The fused image is expected to preserve fine details and maintain high visual fidelity. While diffusion models have demonstrated impressive generative capabilities in image generation, they often suffer from detail loss when applied to image fusion tasks. This issue arises from the accumulation of noise errors inherent in the Markov process, leading to inconsistency and degradation in the fused results. However, incorporating explicit supervision into end-to-end training of diffusion-based image fusion introduces challenges related to computational efficiency. To address these limitations, we propose the Reversible Efficient Diffusion (RED) model—an explicitly supervised training framework that inherits the powerful generative capability of diffusion models while avoiding the distribution estimation. First, we introduce a reversible fusion paradigm within the diffusion process to substantially reduce memory usage, enabling end-to-end training for direct image fusion. Additionally, we integrate a reversible residual block to further reduce memory consumption during training, allowing the model to generate high-quality fusion results. Extensive experimental results demonstrate that RED significantly outperforms state-of-the-art methods across a variety of multi-modal image fusion tasks.

1. Introduction

Multi-modal image fusion is a widely used technique that aims to generate a comprehensive and informative representation by integrating complementary information from diverse source modalities. Representative examples include visible-infrared image fusion (VIF) and medical image fu-

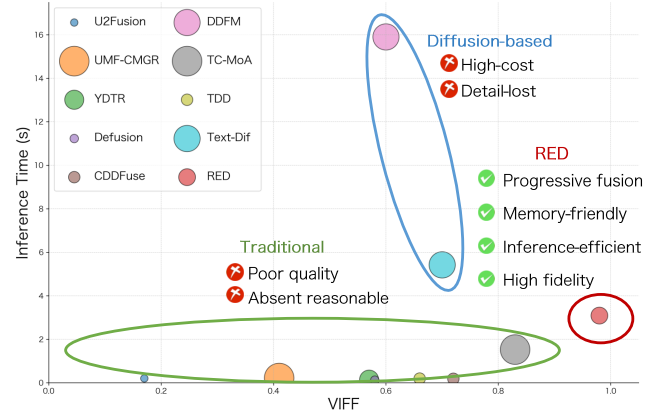


Figure 1. Illustration comparing the proposed RED framework with previous fusion paradigms. The area of each bubble represents the memory usage of the corresponding model. RED demonstrates superior performance while maintaining both low inference time and low memory usage.

sion (MIF). Its primary objective is to produce fused images that preserve and enhance the most salient features of each modality while eliminating redundant or conflicting information. Multi-modal image fusion has been extensively applied in downstream computer vision tasks, including object detection, semantic segmentation, and disease diagnosis, where it provides valuable insights by combining rich information from multiple sensors.

Recent research has explored various fusion techniques, including encoder-decoder fusion, transformer-based fusion, generative adversarial networks (GAN-based) fusion, and more recently, diffusion-based fusion. Among generative models, denoising diffusion models (DMs) have attracted wide attention for modeling complex data via a neural-network-parameterized reverse Markov chain [10]. Latent variants such as Stable Diffusion have achieved impressive image synthesis results [24, 26]. However, im-

age fusion differs from free-form generation and demands faithful preservation of structural details and strict cross-modal consistency. Vanilla DMs are trained with a noise-prediction objective and typically rely on stochastic sampling, and without explicit structural or semantic constraints tied to the source modalities the fused outputs can lose fine details or exhibitin consistencies [30]. Moreover, the multi-step reverse process can accumulate prediction errors across iterations, especially when guidance is weak, introducing artifacts in the final image. These factors limit the direct applicability of off-the-shelf diffusion models to high-fidelity fusion, where explicit structure preservation and modality alignment are critical. Therefore, achieving effective fusion with diffusion models typically calls for explicit loss constraints and reduced sampling stochasticity, rather than relying solely on standard noise-prediction training.

To address the aforementioned challenges, we propose a novel Reversible Efficient Diffusion (RED) for Image Fusion. RED bridges generative diffusion and fusion objectives by enabling end-to-end training under strong, task-aware supervision from both source images and the fused target, resulting in superior performance, as illustrated in Fig. 1. However, naively training diffusion models end to end is often prohibitive on consumer-grade hardware due to memory and compute demands. Inspired by invertible architectures [3, 39], we propose the reversible fusion paradigm that supervises the entire diffusion process with manageable memory. This is achieved by avoiding the storage of intermediate features during forward propagation and instead recomputing them during backpropagation. Furthermore, we incorporate reversible residual blocks [8] into the diffusion backbone, providing additional memory savings while maintaining, and even enhancing, the quality of the fused results. This design makes RED compatible with explicit fusion losses and reduced-stochasticity sampling, aligning the training objective with fusion-specific requirements without incurring prohibitive memory overhead improved the fidelity and modality consistency of the fused results. In summary, the main contributions are as follows:

- We propose a reversible efficient diffusion (**RED**), a novel non-Markovian diffusion training paradigm tailored for image fusion, which leverages supervision from the source images to alleviate noise accumulation and improve structural consistency.
- We introduce a reversible fusion strategy that enables memory-efficient training of RED with alternating iterative fusion. In addition, we incorporate reversible residual blocks to further reduce memory overhead and enhance the quality of the fused outputs.
- Extensive quantitative and qualitative experiments demonstrate the effectiveness and generalizability of RED across both visible-infrared and medical image fusion tasks, while also facilitating improvements in

downstream applications.

2. Related Work

Image Fusion. End-to-end image fusion significantly enhances performance by learning nonlinear mapping relationships between source images. Early approaches primarily employed CNN-based models, which extract local features through hierarchical convolutional layers and integrate multi-source information by designing specific fusion strategies [14, 15, 23, 36, 38]. Transformer-based methods demonstrate superior performance due to the benefits of self-attention mechanisms, making them suitable for image fusion tasks [19, 32], leveraging transformer blocks to capture global dependencies. However, these models are often computationally intensive. To further improve both local and global feature extraction, hybrid CNN-Transformer architectures have been proposed, combining to capture low-level details and high-level semantic [35, 40]. In parallel, state space models such as the Mamba [9] offer promising solutions for modeling long sequences with linear complexity, and have been successfully applied to image fusion tasks, delivering high efficiency at low computational cost [16, 22, 33]. However, these models typically operate in a single training and inference stage, which may limit their ability to fully capture relevant information from source images. Our RED employs an iterative fusion strategy, progressively incorporating new details at each step to enable a more thorough and refined fusion process.

Diffusion-based Image Fusion. Diffusion models have recently emerged as powerful generative frameworks. The DDPM [10] formulates a Markov chain that gradually perturbs data into noise and then reconstructs it via iterative sampling. However, accurate noise estimation typically requires a large number of sampling steps, making inference costly and potentially destabilizing consistency. To mitigate this, more efficient and consistency-preserving samplers such as DDIM [27] and the Improved Diffusion framework [21] reduce the original thousands of steps to fewer than a hundred. The Latent Diffusion Model (LDM) [24] further cuts computation by performing diffusion in a compressed latent space. Nevertheless, the standard DMs training objective focuses on noise prediction for diversity image synthesis, rather than explicitly enforcing the structural fidelity and cross-modal consistency required by image fusion. To address this gap, we propose a new diffusion-based paradigm, RED, tailored to fusion requirements, which optimizes the diffusion backbone end-to-end with explicit fusion constraints and produces fused images directly, aligning the generative objective with modality alignment and structure preservation while maintaining efficiency.

Reversible Neural Networks. Reversible neural networks are a class of architectures capable of mapping observations directly to their underlying true states. NICE [6], a

generative model, learns a nonlinear deterministic transformation of the data, effectively mapping latent variables to a factorized distribution. RevNet [8], a variant of ResNet, achieves comparable accuracy while reducing memory usage by storing intermediate values only during backpropagation. Prior studies [2, 7] have shown that reversible neural networks serve as powerful analytical tools for identifying multi-modal structures in parameter space, uncovering parameter correlations, and detecting unrecoverable parameters. This memory-efficient architecture makes reversible networks particularly well-suited to generative modeling, as normalizing flows enable exact, likelihood-based training.

3. Preliminary

DDIM. The denoising diffusion implicit model (DDIM) [27] proposed a more efficient class of iterative sampling based on DDPM [10]:

$$x_{t-1} = \sqrt{\bar{\alpha}_{t-1}} x_0 + \sqrt{1 - \bar{\alpha}_{t-1}} \epsilon_t \quad (1)$$

where $x_0 = (x_t - \sqrt{1 - \bar{\alpha}_t} \epsilon_t) / \sqrt{\bar{\alpha}_t}$ denotes the current denoised image. This diffusion-based framework unifies principles from hierarchical variational inference and score-based generative modeling, offering stable training and high-quality sample generation.

Reversible Residual Block. RevNets [8] can be constructed using reversible residual blocks, which are designed to be mathematically invertible, thereby reducing memory consumption during training. Building on this concept, the Re²TAL [39] further enhances reversibility and computational efficiency by rewiring connections, enabling the lightweight fine-tuning of consecutive residual modules within the same stage. These modules are rewired to ensure reversibility, with each residual connection skipping an additional block, denoted as F and G . The following equation formally describes the rewiring process:

$$\begin{cases} y_1 = x_0 \\ x_1 = F(x_0) + y_0 \end{cases} \Rightarrow \begin{cases} y_2 = x_1 \\ x_2 = G(x_1) + y_1 \end{cases} \quad (2)$$

These equations are reversible, allowing recovery of inputs x_1, y_1 from x_2, y_2 , and subsequently x_0, y_0 from x_1, y_1 . The corresponding inverse computation is given by:

$$\begin{cases} x_0 = y_1 \\ y_0 = x_1 - F(x_0) \end{cases} \Leftarrow \begin{cases} x_1 = y_2 \\ y_1 = x_2 - G(x_1) \end{cases} \quad (3)$$

This reversible structure allows efficient memory usage during training by eliminating the need to store intermediate activations, making it particularly suitable for deep and resource-constrained networks.

4. Method

The goal of image fusion is to generate a fused image f from visible v and infrared i images, where $i, v, f \in \mathcal{R}^{C \times H \times W}$. H and W represent the height and width, and C signifies the channels.

4.1. End-to-end Diffusion Model for Image Fusion

We propose an end-to-end training strategy to address the inherent ambiguities in measurements and the task gap present in the diffusion process. To this end, we introduce a novel diffusion-based image fusion framework that reformulates the DDIM [21] sampling procedure as a T -layer neural network, denoted as $\mathcal{F} = \mathcal{F}_1 \circ \mathcal{F}_2 \circ \dots \circ \mathcal{F}_T$, where each layer \mathcal{F}_t represents a sequential sampling step. Moreover, the coefficients α_{t-1}^T are jointly fine-tuned [5]. This layered structure enables progressive fusion, allowing the model to iteratively refine the fused image. To improve training efficiency, we adopt Latent Diffusion Models (LDMs) as the backbone and retain only the outermost two layers. The up-sampling and down-sampling operations, such as pixel-shuffle and unpixel-shuffle, are used to replace the role of the variational autoencoder (VAE). The framework is trained to minimize the discrepancy between the estimated output $f = \mathcal{F}(x, y)$ and the ground truth (x, y) using standard loss functions commonly applied in image fusion tasks. This design enhances adaptability and overall performance, enabling the framework to generalize across diverse fusion scenarios.

4.2. Reversible Image Fusion

To implement end-to-end diffusion, we designed a reversible image fusion framework for efficient fusion. Inspired by [39], we reformulate the rewiring process for image fusion, enabling progressive fusion. The coupling blocks consist of a diffused process with $f = \mathcal{F}(x, y)$, the inverse is the $[x, y] = \mathcal{F}^{-1}(f)$. In the following, we mathematically formulate the reversible modules. Firstly, we propose wiring to enable invertibility by introducing new connections into the sampling steps. Each input of the sampling step \mathcal{F}_t is connected with the output of the \mathcal{F}_{t-1} . To represent the backpropagation process of the reverse process, it is beneficial to rephrase the forward (left) and reverse (right) computations in the following manner.

$$\begin{cases} f_{t+1} = f_{t-1} + \mathcal{F}_t(f_t) \\ f_{t-1} = f_t \\ f_t = f_{t+1} \end{cases} \Leftrightarrow \begin{cases} f_t = f_{t-1} \\ f_{t+1} = f_t \\ f_{t-1} = f_{t+1} - \mathcal{F}_t(f_t) \end{cases} \quad (4)$$

Note that, even though the $f_{t-1} = f_t$ in Eq. 4, the two variables represent distinct nodes of the computation graph, so the total derivatives f_{t-1} and f_t are different.

In the forward process, we cache the final output of wired layers and the intermediate features are freed up. By iteratively applying Algorithm 1, backpropagation can be performed across a sequence of reversible blocks using only the activations and their derivatives from the topmost layer. The complete diffusion process becomes reversible when

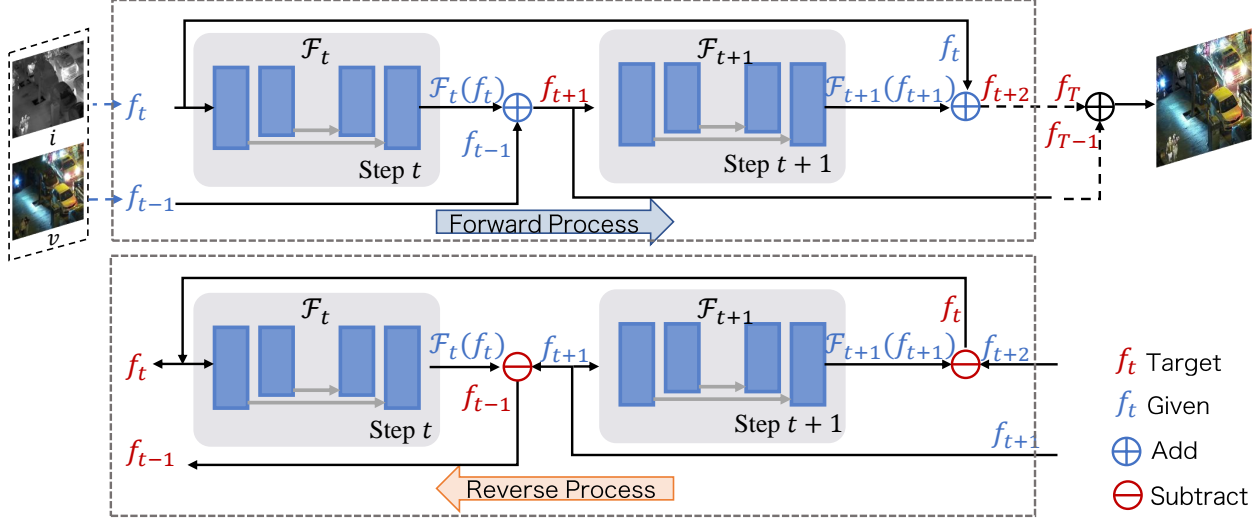


Figure 2. Workflow of the proposed RED model. The illustration depicts the reversible diffusion process and the knowledge-guidance module. The backbone adopts a U-Net architecture, where the standard residual blocks are replaced by reversible residual blocks.

multiple reversible modules are stacked consecutively in a network (Fig. 2). In this configuration, we execute the back-propagation from (f_0, f_1) back to (i, v) , reconstruction begins at the final module, with each module’s input sequentially recovered using Eq. 2. After computing the loss function \mathcal{L} . The final fusion output $f = w f_T + (1 - w) f_{T-1}$, here the w is a learnable parameter. Note that this approach can be applied to arbitrary diffusion models without the need to design new neural networks. It significantly saves memory, time, and computation, improving reconstruction performance.

The U-Net architecture [25] is commonly used as a noise estimator in diffusion models. It includes a series of down-sampling and mirrored up-sampling operations with skip connections. These blocks consist of residual and attention blocks, which are memory-intensive. To further improve memory efficiency, we extend the concatenation of the reversible residual block to the U-Net blocks at each step, as in RevNet [8], as shown in Eq. 2 and Eq. 3. We group and concatenate consecutive transformation blocks within each block, making them reversible. During training, we clear all inputs and intermediate activations of these grouped blocks from memory, retaining only the features of the first and last convolutions and skip branches for backpropagation. This reversible design reduces memory usage and enables our method to train on consumer GPUs [5].

4.3. Loss Function

As an end-to-end (E2E) framework, the loss functions used to train RED include SSIM loss, MAE loss, and maximum gradient loss. Detailed, the SSIM loss encourages the model to preserve important structural features, leading to more perceptually realistic results. It can be formulated as:

$\mathcal{L}_{\text{SSIM}} = 2 - (\text{SSIM}(i, f) + \text{SSIM}(v, f))$. The MAE loss aims to minimize the pixel-level differences and improve the visual similarity between the source images and the fused image denoted as: $\mathcal{L}_1 = \|i - f\|_1 + \|v - f\|_1$. The maximum gradient loss helps improve the perceptual quality of images by focusing on maintaining edge sharpness. It can be defined as: $\mathcal{L}_{\text{grad}} = \frac{1}{HW} \|\nabla f - \max(\nabla v, \nabla i)\|_1$, here ∇ represents the Sobel operator, which extracts edge information from the image. The total loss function is defined as $\mathcal{L} = \mathcal{L}_{\text{SSIM}} + \mathcal{L}_1 + \mathcal{L}_{\text{grad}}$. This formulation provides explicit supervision from the source images and the fused image, thereby enhancing the fidelity of the fusion results.

5. Experiments

5.1. Setup

Implementation Details. We conduct experiments on three image fusion datasets: LLVIP [11], MSRS [28], and M³FD [18], using PyTorch on a machine equipped with two NVIDIA GeForce RTX A6000 GPUs. Additionally, we perform medical image fusion experiments on the Whole Brain Atlas dataset from Harvard Medical School [12] as a complementary evaluation. The model is trained on the LLVIP training set and evaluated following the TC-MoA [42]. To assess the generalization ability, the model trained on LLVIP is directly evaluated on the MSRS, M³FD, and Harvard Medical datasets without fine-tuning, using the same evaluation metrics. During training, we set $T = 2$, image pairs are randomly cropped into 128×128 patches, with a batch size of 4. The model is optimized using the Adam optimizer with parameters $\beta_1 = 0.9$ and $\beta_2 = 0.999$.

Evaluation Metrics. We evaluated the fusion results in

Table 1. Quantitative comparison with SOTAs. The **bold**/underline indicates the best and runner-up.

Visible-Infrared Image Fusion on LLVIP Dataset					Visible-Infrared Image Fusion on MSRS Dataset					
	EI	AG	SF	$Q^{AB/F}$	VIFF	EI	AG	SF	$Q^{AB/F}$	VIFF
UMF-CMGR [31]	8.43	3.40	11.89	0.31	0.39	6.32	2.41	7.47	0.26	0.41
YDTR [29]	8.91	3.72	13.82	0.35	0.47	6.55	2.48	7.72	0.35	0.57
DeFusion [17]	9.94	3.87	12.02	0.42	0.58	7.13	2.66	8.05	0.45	0.58
U2Fusion [34]	11.48	4.53	14.25	0.43	0.48	7.78	2.96	8.27	0.15	0.17
CDDFuse [40]	13.31	5.40	18.50	0.58	0.66	10.07	3.78	11.57	0.58	0.72
DDFM [41]	8.10	3.32	11.89	0.35	0.59	5.37	2.04	6.44	0.29	0.60
TC-MoA [42]	<u>14.18</u>	<u>5.69</u>	18.79	0.60	<u>0.71</u>	8.55	3.15	9.19	<u>0.61</u>	<u>0.83</u>
TTD [4]	13.83	5.44	<u>19.18</u>	<u>0.65</u>	0.69	9.71	3.71	11.53	0.55	0.66
Text-DiFuse [37]	12.56	4.85	15.53	0.40	0.52	10.36	<u>3.84</u>	11.51	0.44	0.70
RED (Ours)	14.74 (+0.56)	5.91 (+0.22)	19.29 (+0.11)	0.74 (+0.09)	0.93 (+0.22)	10.39 (+0.03)	3.90 (+0.06)	11.57 (-0.00)	0.70 (+0.09)	0.98 (+0.15)
Visible-Infrared Image Fusion on M3FD Dataset					Medical Image Fusion on Harvard Dataset					
	EI	AG	SF	$Q^{AB/F}$	VIFF	EI	AG	SF	$Q^{AB/F}$	VIFF
UMF-CMGR [31]	7.75	2.98	8.90	0.40	0.60	16.22	6.32	22.66	0.41	0.37
YDTR [29]	8.68	3.36	10.22	0.48	0.62	15.25	5.90	21.64	0.41	0.52
DeFusion [17]	6.89	2.62	7.48	0.34	0.53	16.24	6.14	21.79	0.51	0.52
U2Fusion [34]	8.17	3.11	9.12	0.38	0.49	16.23	6.12	21.18	0.46	0.46
CDDFuse [40]	12.45	4.80	14.71	0.52	0.58	19.53	7.44	<u>26.24</u>	0.62	<u>0.67</u>
DDFM [41]	8.17	3.11	9.12	0.38	0.49	13.96	5.40	20.76	0.35	0.43
TC-MoA [42]	12.03	4.61	13.81	0.63	0.78	16.52	6.23	21.21	<u>0.64</u>	<u>0.53</u>
TTD [4]	<u>12.88</u>	<u>4.98</u>	14.84	0.60	0.64	<u>19.77</u>	7.80	28.97	0.63	0.49
Text-DiFuse [37]	7.51	2.81	8.47	0.15	0.16	17.99	6.76	24.27	0.45	0.48
RED (Ours)	13.04 (+0.16)	5.00 (+0.02)	<u>14.81</u> (-0.03)	0.70 (+0.07)	0.93 (+0.15)	20.24 (+0.47)	<u>7.67</u> (-0.13)	26.14(-1.83)	0.71 (+0.07)	0.69 (+0.02)

both quantitative and qualitative. Qualitative evaluation is primarily based on subjective visual assessments conducted by individuals. We expect the fused image to exhibit rich texture details and abundant color saturation. Objective evaluation focuses primarily on measuring the quality assessments of individual fused images and their deviations from the source images. For different task scenarios, the same evaluation metrics are used, specifically, we employ five metrics including edge intensity (EI), average gradient (AG), spatial frequency (SF), gradient-based similarity measurement ($Q^{AB/F}$) and visual information fidelity for fusion (VIFF) for evaluation metrics.

5.2. Comparison with SOTA methods

Competing Methods. We compared our method with seven recent competing methods, including U2Fusion [34], UMF-CMGR [31], YDTR [29], DeFusion [17], CDDFuse [40], DDFM [41], TC-MoA [42], TTD [4], and Text-DiFuse [37].

Quantitative Comparisons. As shown in Table 1, the evaluation metrics demonstrate that our fusion results consistently outperform existing methods. Our approach excels by ranking first or second in all evaluated metrics, showcasing remarkable performance across various VIF datasets. Notably, the competitive values in the EI, AG and SF metrics reflect the superior detail preservation and enhanced texture quality achieved by RED. The highest values of $Q^{AB/F}$ and

VIFF also highlight that our fusion outputs exhibit the highest correlation with human visual perception, underscoring their closer alignment with human perception. This ensures that the generated images are not only perceptually accurate but also retain the integrity of the original source information. The outperformance across diverse datasets reinforces the effectiveness and robustness of RED in complex application scenarios, indicating that comprehensive information has been preserved. Meanwhile, MIF achieves the best performance in EI, $Q^{AB/F}$, and VIFF, as well as the second-best result in AG, demonstrating RED’s adaptability across different scenarios and tasks to produce high-quality results.

Qualitative Comparisons. Qualitative comparison results with state-of-the-art (SOTA) image fusion methods are shown in Fig.3. In rows 1–2 of Fig.3, our method effectively preserves shadow details of the tree in the dark visible-light regions while simultaneously retaining the texture of the floor tiles in the infrared image. This is particularly evident when compared to Text-DiFuse, demonstrating the effectiveness of our image-level constraints. In the red box of In rows 3–4 of Fig.3, highlighted in the red box, our method excels in retaining more infrared information in overexposed sky regions, where other methods typically lose detail. This dual preservation of information is critical for maintaining scene context in both modalities benefited from the iterative fusion process, which enables RED to adapt effectively to complex scenarios. In Fig. 3 row

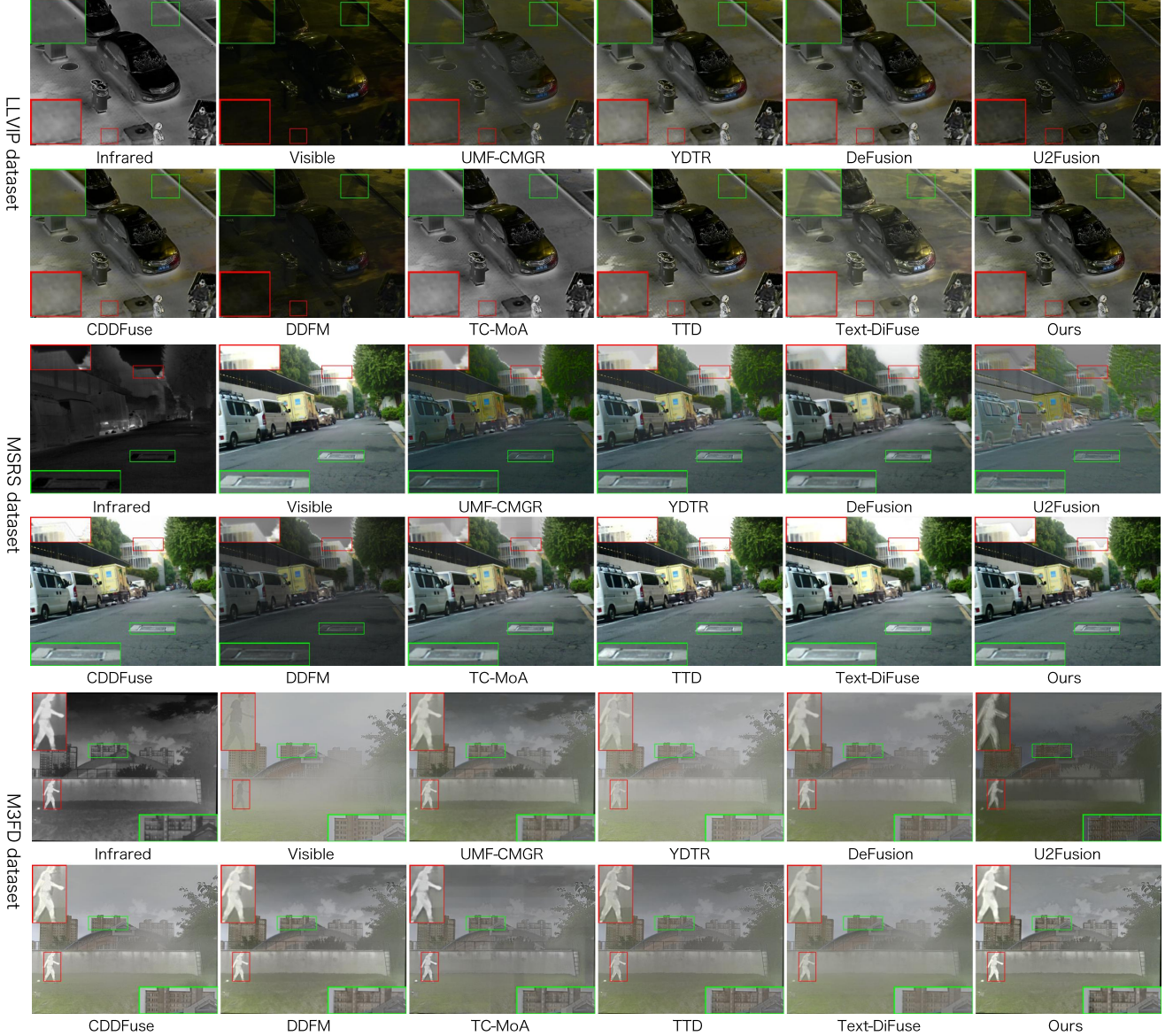


Figure 3. Qualitative comparisons of SOTA methods in the LLVIP, MSRS, M^3 FD datasets.

5-6, our approach demonstrates robustness in the presence of smoke, resulting in fused images with superior clarity and contrast compared to other methods. Moreover, RED achieves the best results in the MIF scenario, showing the highest contrast and most distinct structural features shown in Fig. 4, which highlights its strong task adaptability.

5.3. Ablation Study

Qualitative and Quantitative Analysis. We conduct a series of ablation studies on the LLVIP dataset to evaluate the effectiveness of the proposed modules in RED. Table 2 presents several variants of RED, each with a specific module ablated. Specifically, Reverse I denotes the reversible fusion strategy, Reverse II refers to the reversible residual

block, and without DDPM indicates the exclusion of the denoising process. Without the reversible fusion strategy, the model runs with huge memory during training, indicating that this component is essential for enabling end-to-end training under limited memory budgets. This confirms its critical role in reducing memory consumption via reversible computation. When Reverse I is included but Reverse II is removed, the model achieves a competitive PSNR of 19.35 and EI of 14.71, highlighting that reversible residual blocks are essential for structural fidelity and perceptual quality. Adding Reverse II results in minimal impact on memory usage, demonstrating the strong contribution to visual consistency. However, the most significant improvement is achieved when all components, including the

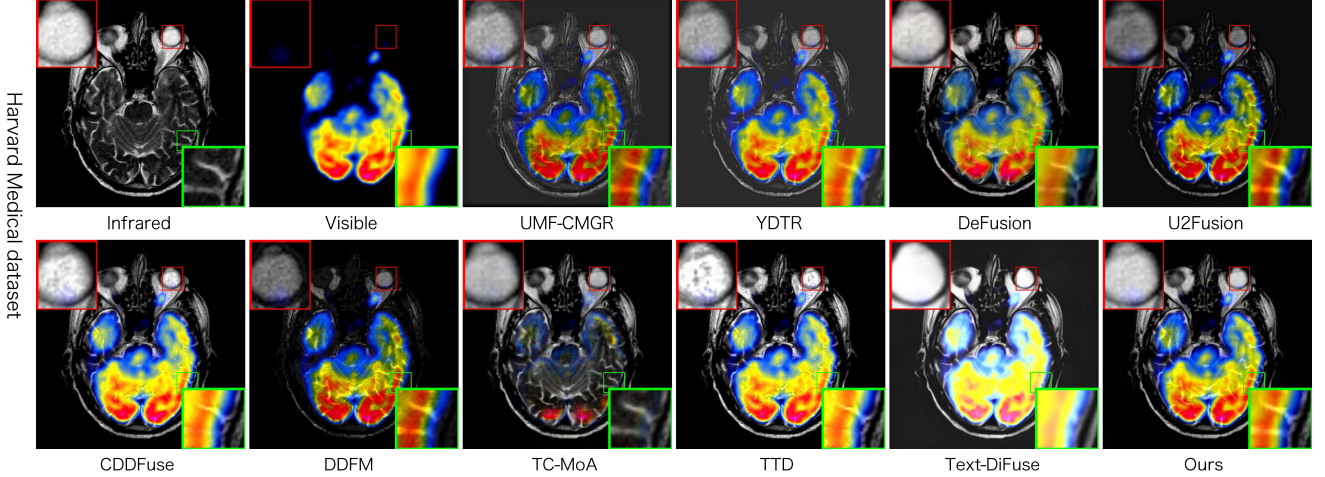


Figure 4. Qualitative comparisons of SOTA methods in Harvard Medical dataset.

Table 2. Ablation studies on the LLVIP dataset. **Bold** indicates the best performance. "Mem." denotes memory usage, and "Inf." refers to inference time. OOM indicates out-of-memory.

Reverse I	Reverse II	DDIM	EI	AG	PSNR	$Q^{AB/F}$	VIFF	Mem. (GB)	Inf. (s)
-	✓	✓	14.44	5.79	19.01	0.73	0.91	20.1	1.09
✓	-	✓	14.71	5.90	19.35	0.74	0.92	9.44	1.09
✓	✓	-	14.47	5.80	19.07	0.73	0.92	9.44	1.10
✓	✓	✓	14.74	5.91	19.29	0.74	0.93	7.14	1.30

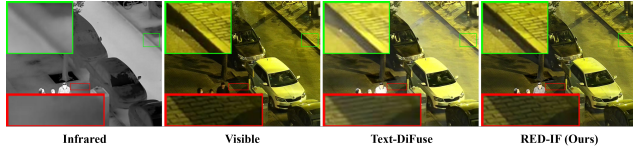


Figure 5. Visualization of representative details lost exhibited by Text-DiFuse.

denoising diffusion process, are activated. In this configuration, RED achieves the best overall performance with a PSNR of 19.29, AG of 5.91, EI of 14.74 and the highest VIFF of 0.93, indicating enhanced information preservation. Furthermore, we provide more ablation analysis in the Appendix. These all validate the effectiveness of each proposed component. Overall, RED achieves superior performance with substantial memory efficiency, underscoring the efficacy of our architectural design.

The RED model applies direct supervision to both the source images and the fused output, resulting in impressive performance. But why does image-level supervision lead to such encouraging fusion results? The key lies in the explicit alignment between input modalities and the target image, which helps preserve fine details and semantic consistency. In contrast, diffusion models trained with weak or implicit supervision tend to interpolate smoothly between data modes seen during training [20], which can lead to over-smoothed outputs and a loss of fine structures. Moreover, recent studies have shown that minor inconsis-

Table 3. Comparison of object detection on LLVIP dataset. **Bold** indicates the best.

Method	Precision	Recall	mAP@.5	mAP@.5:.95
U2Fusion [34]	0.938	0.898	0.954	0.631
UMF-CMGR [31]	0.946	0.886	0.950	0.637
YDTR [29]	0.946	0.905	0.958	0.631
DeFusion [17]	0.945	0.905	0.959	0.629
CDDFuse [40]	0.948	0.899	0.955	0.631
DDFM [41]	0.952	0.904	0.960	0.630
TC-MoA [42]	0.939	0.914	0.961	0.637
TTD [4]	0.944	0.894	0.952	0.630
Text-DiFuse [37]	0.937	0.874	0.939	0.596
Dream-IF (Ours)	0.949	0.906	0.962	0.639

tencies in conditions can be progressively amplified during iterative sampling [1], leading to the accumulation of artifacts and deviations from real data distribution. These behaviors are particularly problematic in Markovian diffusion processes, where each step depends solely on the previous state, exacerbating error accumulation. Such issues are clearly observed in Text-IF, as illustrated in Fig. 5, which demonstrates both detail degradation (green box) and structural distortions (red box). By contrast, RED benefits from strong image-level supervision, which anchors the fusion process to ground-truth semantics and structures, thereby mitigating error propagation and yielding more refined and faithful fusion results.

5.4. Downstream VIF Application

In this section, we provide an evaluation of the downstream performance on the LLVIP dataset, taking object detection as an example, utilizing the YoloV11 [13] detection backbone. The model is trained for a total of 200 epochs using the SGD optimizer, with an initial learning rate set to 0.01. For each comparison method, we retrain the model by incorporating the fusion results obtained from their respective

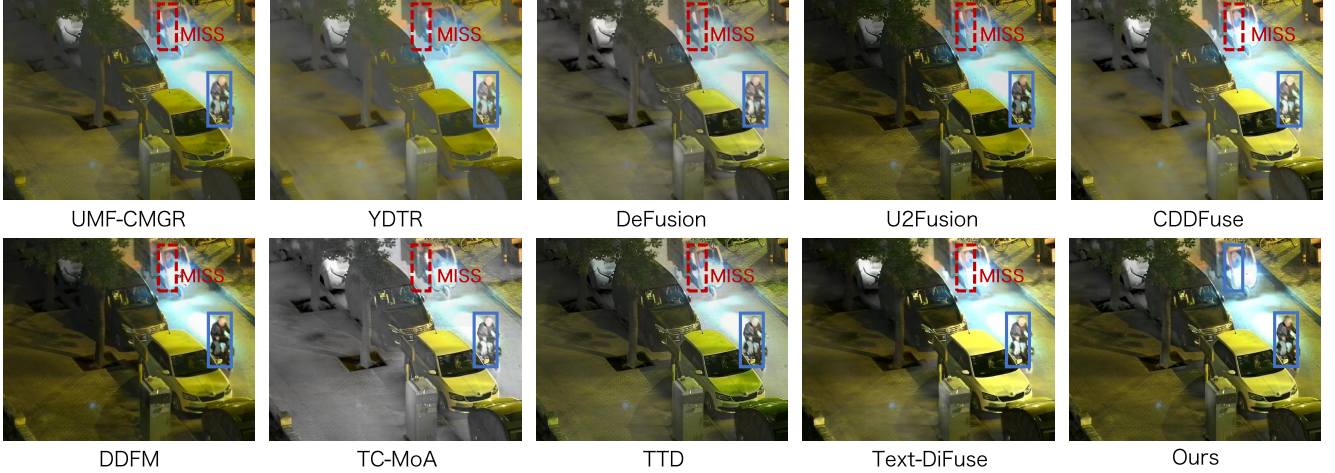


Figure 6. Visualization comparing SOTA methods on the object detection task.

methods, ensuring a fair comparison across all approaches. The evaluation is conducted using a comprehensive set of metrics, including precision, recall, mean average precision at IoU 0.5 (mAP@0.5), and mean average precision at IoU 0.5:0.95 (mAP@0.5:95). The results of these evaluations are systematically presented in Table 3, indicating that RED consistently outperforms all other comparison methods across all evaluation metrics, particularly mAP@0.5:95 increased by 0.019 than the suboptimal. Fig. 6 presents a visualization in which RED successfully detects a person under strong illumination—an instance where other methods fail. Additional visualizations are provided in the appendix. This superior performance highlights RED’s effectiveness in enhancing detection tasks and demonstrates its robust capability to adapt to downstream applications.

6. Discussion

How Much Iterative Training? We further investigate the impact of the number of iterative steps on model performance, as shown in Fig. 7 and visualize the intermediate output in the Appendix. The results indicate that increasing the number of iterations generally enhances performance. However, the marginal gain diminishes with additional steps, suggesting a saturation effect. Moreover, computational resource consumption increases approximately linearly with the number of iterations, revealing a trade-off between performance and efficiency. To better understand the advantages of end-to-end supervision in RED, we compare its VIFF scores with those of the diffusion-based image fusion method Text-DiFuse [37] with randomly selecting a sample, as shown in Fig. 8. RED achieves high fidelity even at early stages of the diffusion process, with performance improving steadily over subsequent iterations. In contrast, Text-DiFuse exhibits a slower and less efficient increase in fidelity, reflecting a more delayed fusion process.

By discarding the traditional Markov-based framework,

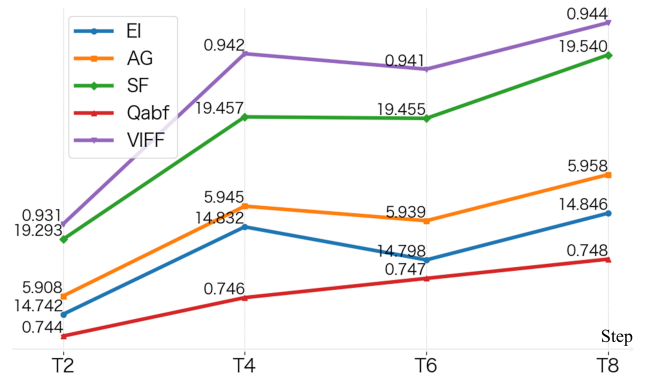


Figure 7. Quantitative results at different diffusion steps. Values are scaled for visualization.

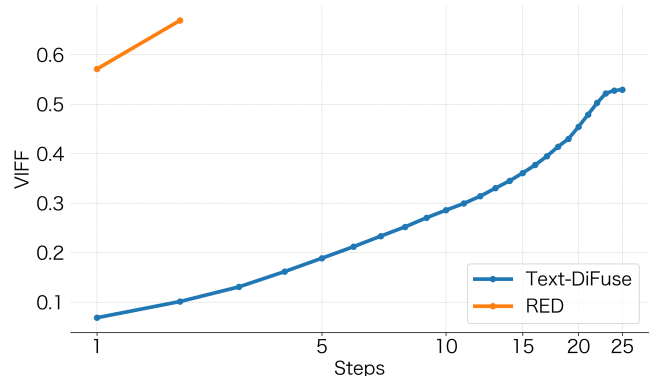


Figure 8. Comparison VIFF at different diffusion steps with Text-DiFuse.

RED introduces direct supervision between the source images and the fused output. This design enables the model to achieve high-quality results with fewer diffusion steps, making it more suitable for image fusion tasks that demand both accuracy and computational efficiency.

7. Conclusion

In this paper, we propose an end-to-end diffusion model for image fusion that leverages strong supervision to mitigate the inconsistency generation in diffusion models. We employ a reversible architecture to enable end-to-end training while significantly reducing memory consumption. Furthermore, our exploration of iterative steps demonstrates the model’s capabilities and inspires a novel paradigm for image fusion. Empirical results show that RED outperforms competing methods, achieving superior performance across various datasets. In future work, we aim to develop automatic step selection strategies to balance computational cost and performance metrics, thereby enabling more practical and effective image fusion.

Reversible Efficient Diffusion for Image Fusion

Supplementary Material

8. Technical Appendices and Supplementary Material

8.1. More Details of Reversible Fusion

Our RED is modality-agnostic. In this work, we instantiate it with two inputs by initializing $f_0 = v$ and $f_1 = i$, where v and i denote the visible and infrared images, respectively. The fused image is produced from the final states f_T and f_{T-1} . The reverse starts from f_T and f_{T-1} obtained in the forward trajectory. As detailed in Algorithm 1 summarizes both the forward and backward procedures of the reversible fusion module, including how intermediate states are recomputed to achieve memory efficiency. , the reversible updates deterministically reconstruct earlier states (f_t, f_{t-1}) from (f_{t+1}, f_t) . During backpropagation, we recompute these intermediate states instead of storing activations from the forward pass, which substantially reduces memory usage, which is a key benefit under limited GPU budgets.

Algorithm 1 RED: The Function BLOCK REVERSE

Input: $:(f_t, f_{t+1}), (\bar{f}_t, \bar{f}_{t+1})$

Output: $: f_{t-1}$, and $\bar{\omega}_{\mathcal{F}}$

- 1: $f_{t-1} \leftarrow f_{t+1} - \mathcal{F}_t(f_t)$ \triangleright Get the old state by subtracting a function.
- 2: $\bar{f}_{t-1} \leftarrow \bar{f}_{t+1} + \left(\frac{\partial \mathcal{F}}{\partial f_t} \right)^\top \bar{f}_{t-1}$ \triangleright Update gradient for current using backward rule.
- 3: $\bar{\omega}_{\mathcal{F}} \leftarrow \left(\frac{\partial \mathcal{F}}{\partial \omega_{\mathcal{F}}} \right)^\top f_t$ \triangleright Get the gradient of the parameters.
- 4: $f_t \leftarrow f_{t-1}$ \triangleright Copy the old state to current.
- 5: $f_{t+1} \leftarrow f_t$ \triangleright Copy current state to next.
- 6: return $f_{t-1}, \bar{f}_{t-1}, \bar{\omega}_{\mathcal{F}}$ \triangleright Give back the state and gradients.

8.2. More Ablation Studies

Fig. 9 shows the results reconstruction after DDPM. In the RED ablation study, we conducted experiments using DDPM to highlight the differences between RED and a simple cascaded model. Furthermore, visualizations demonstrate that even a single-step denoising operation within the diffusion framework can substantially improve the quality of the generated images.

RED employs an iterative fusion strategy, progressively refining the fusion process, where f_T is the refined version of f_{T-1} . The final fused image is obtained using $f = w \cdot f_T + (1 - w) \cdot f_{T-1}$, where w is a learnable parameter optimized during training and used during infer-

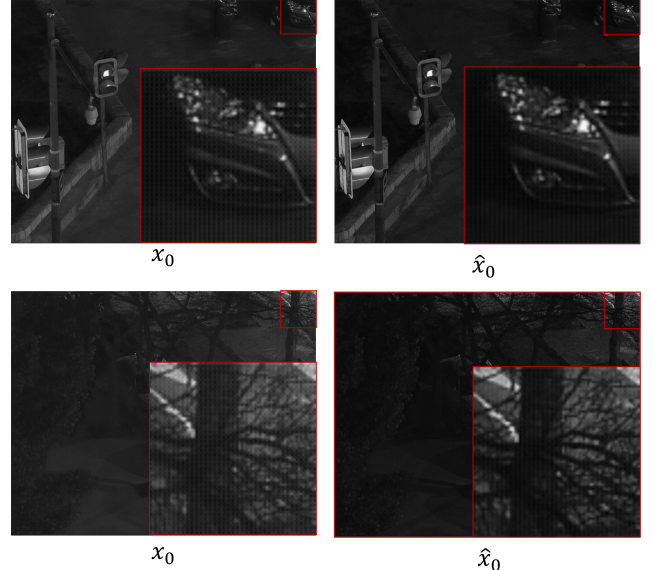


Figure 9. Visualization of image reconstruction results after applying DDPM.

ence, which supplements the information from the previous step. Table 7 presents additional ablation results regarding the learnable parameter w . Ablation (1) demonstrates that the learnable parameter w can adaptively determine an appropriate fusion weight, effectively combining results of different degrees. Table 4 shows the values of w across different training epochs and fusion steps, illustrating its interpretability. The w starts at 1 and slightly decreases with the training. Since f_T is much more important than f_{T-1} , w places a stronger emphasis on f_T . Over time, RED learns to integrate both f_T and f_{T-1} , with f_T continuing to dominate the final fusion process. f_T is the refined version of f_{T-1} and shows higher performance compared to f_{T-1} . The fused output, integrating both images with the learned weight, further enhances performance.

Furthermore, we replaced the pixel and pixel shuffle operations (used for down- and up-sampling, respectively) with convolution and transposed convolution layers, as commonly done in VAE. However, convolution-based sampling is more difficult to train, prone to collapse, and introduces additional learnable parameters. Ablation (2) shows that RED performs better with pixel shuffle-based sampling, indicating that this approach is more stable and effective for fusion tasks.

8.3. More Preliminaries

DDPM. Denoising Diffusion Probabilistic Models (DDPM) construct a generative framework that has demon-

Table 4. Evolution of fusion weight w and VIFF scores across training epochs.

Training epoch	0 (initial)	2	4	6	8	10
w	1.0000	0.9662	0.9617	0.9595	0.9579	0.9567
f_{T-1} (VIFF)	0.4567	0.4937	0.4937	0.4686	0.4475	0.4375
f_T (VIFF)	0.8650	0.9062	0.9277	0.9336	0.9329	0.9298
f (VIFF)	0.8661	0.9078	0.9293	0.9360	0.9350	0.9320

Table 5. Ablation on the number of diffusion steps T .

Setting	EI	AG	SF	QABF	VIFF	Mem.(GB)	Inf.(s)	Tr.(h)
T=2 (2 \times)	14.161	5.524	19.014	0.780	1.054	7.14	27.0	40
T=2	14.742	5.908	19.293	0.744	0.931	7.14	1.3	40
T=4	14.832	5.945	19.457	0.746	0.942	7.15	2.7	80
T=6	14.798	5.939	19.455	0.747	0.941	7.15	5.9	120
T=8	14.846	5.958	19.540	0.748	0.944	7.14	8.0	160

strated remarkable performance in various image synthesis tasks. The model consists of a forward diffusion process that gradually corrupts a clean sample with Gaussian noise, and a corresponding reverse denoising process that iteratively reconstructs the original data. In the forward process, a clean data sample $x_0 \sim p_{\text{data}}(x)$ is transformed into a noisy latent variable x_T over T steps, discrete time steps according to the following stochastic equation:

$$x_t = \sqrt{\alpha_t}x_{t-1} + \sqrt{1 - \alpha_t}\epsilon_t, \quad \epsilon_t \sim \mathcal{N}(0, I) \quad (5)$$

with $\alpha_t := 1 - \beta_t$, and $\{\beta_t\}_{t=1}^T$ is a predefined noise schedule. This formulation admits a closed-form solution for arbitrary time steps:

$$x_{t-1} = \frac{1}{\sqrt{\bar{\alpha}_t}}(x_t - \frac{\beta_t}{\sqrt{1 - \bar{\alpha}_t}}\tilde{\epsilon}), \quad \bar{\alpha}_t = \prod_{i=1}^t \alpha_i, \quad (6)$$

where $\tilde{\epsilon} = \epsilon_t(x_t, t)$ estimated noise with a neural network. σ_t is the standard deviation within the sampling process. The reverse process learns a parameterized conditional distribution $p_{\theta}(x_{t-1}|x_t)$ that approximates the true posterior of the denoising process. To achieve this, the model is trained to predict the noise term ϵ using a neural network $\epsilon_{\theta}(x_t, t)$ by minimizing the following objective:

$$\min_{\theta} \mathbb{E}_{x_0, \epsilon, t} [\|\epsilon - \epsilon_{\theta}(x_t, t)\|^2] \quad (7)$$

Once trained, the model can generate new samples by starting from a noise vector $x_T \sim \mathcal{N}(0, I)$ and applying the learned reverse process iteratively.

8.4. More Implementation Details

We use Stable Diffusion v1.5 (SD 1.5) as the backbone, with most of the blocks pruned to reduce computational complexity. The RED model is initialized with the pre-trained parameters from SD v1.5 and fine-tuned with $T = 2$ diffusion steps, a batch size of 20, and 10 training iterations on a single NVIDIA A6000 GPU (38 GB memory). The w is initialized by 1.

8.5. More Details about Datasets

Below, we provide a detailed description of each dataset:

LLVIP [11] is a visible-infrared paired dataset for low-light vision tasks. It contains 15,488 pairs, most of which were captured in very dark scenes. All images are strictly aligned in both time and space.

MSRS [28] is a multi-spectral dataset for infrared and visible image fusion, containing 1,444 pairs of high-quality, aligned infrared and visible images. It is derived from the MFNet dataset, with 715 daytime image pairs and 729 nighttime image pairs collected after removing misaligned pairs.

M3FD [18] is constructed using a synchronized acquisition system equipped with a binocular optical camera and a binocular infrared sensor. It includes 4,200 image pairs for training and 300 independent scenes for testing. All visible images are calibrated using the system’s internal parameters, while infrared images are artificially distorted via a homography matrix to simulate real-world challenges. The dataset is particularly valuable for evaluating the generalization capability of fusion methods across diverse scenarios.

8.6. More Visualization of Results

Additional visual comparisons are presented in Fig. 10. RED preserves texture details more effectively than Text-DiFuse, another diffusion-based method. This advantage stems from RED’s design, which incorporates direct supervision into the diffusion process. Compared with other methods, RED consistently demonstrates strong performance in preserving information across both high-light and low-light regions in all three infrared and visible-light datasets. This capability is enabled by RED’s iterative optimization strategy, which progressively refines the fusion process. By leveraging the complementary strengths of both modalities, RED generates the most balanced and visually coherent fused images.

Table 6. Quantitative comparison of diffusion-based methods.

Method	EI	AG	SF	QABF	VIFF	Mem.(GB)	Tr.(h)
CCF	7.10	5.02	16.83	0.42	0.50	—	—
Text-DiFuse	12.56	4.85	15.53	0.40	0.52	22.8	381
LFDT-Fusion	14.26	5.71	18.96	0.72	0.89	11.8	44
RED (ours)	14.74	5.91	19.29	0.74	0.93	7.14	40

Table 7. Ablation studies on the LLVIP dataset. **Bold** indicates the best performance. (1) denotes the variant without the learnable parameter w ; (2) replaces the up- and down-sampling operations with convolution and transposed convolution; (3) corresponds to the RED model.

	EI	AG	PSNR	$Q^{AB/F}$	VIFF
(1)	14.58	5.85	19.20	0.74	0.93
(2)	14.52	5.82	19.03	0.74	0.93
(3)	14.74	5.91	19.29	0.74	0.93

8.7. More Visualization of Downstream

We show some visual samples of object detection in the LLVIP dataset in Fig. 11. RED also performs effectively in downstream tasks such as object detection. It successfully detects objects near occluded or cluttered edges—areas often missed by other methods, and accurately identifies dense, complex crowd regions. These visual results demonstrate that RED significantly improves detection accuracy in challenging scenarios.

8.8. Analysis of Intermediate Outputs

f_T is a refined state of f_{T-1} and empirically achieves higher performance than f_{T-1} . The final fused image \hat{y} integrates information from both states via learned fusion weights w , further improving perceptual quality and cross-modal consistency. Figure 12 visualizes the intermediate states f_{T-1} and f_T . As diffusion progresses, information from one modality is progressively injected into the other, yielding a coherent representation; the progressive fusion process gradually integrates complementary modality-specific details into a single, comprehensive image.

8.9. Comparison With Diffusion-based Methods

As shown in Table 6, we report a quantitative comparison against recent latent-diffusion-based fusion methods, including CCF (training-free), Text-DiFuse (built on DDFM), and LFDT-Fusion (LDM-based). RED consistently outperforms these latent-diffusion baselines.

We attribute RED’s gains to its non-Markov reverse process and reversible fusion framework, which together improve fidelity and information preservation in the fused images. In addition, RED offers notable memory efficiency during training: the reversible mechanism allows us to recompute intermediate states in backpropagation instead of

storing them, reducing GPU memory usage at a given batch size and improving overall training efficiency. In terms of wall-clock performance, RED’s training speed is comparable to LFDT-Fusion: our end-to-end formulation converges quickly, whereas LFDT-Fusion incurs extra steps due to its diffusion procedure, leading to longer training times. This time–memory trade-off stems from our reversible design, which intentionally spends additional computation to save memory.

In summary, RED achieves superior accuracy while using fewer computational resources than current diffusion-based fusion methods.

8.10. More exploration

As detailed in the main text and illustrated in Fig. 7 (Page 9), we further analyzed model performance under increased diffusion steps. The results in Table 5 indicate a general performance improvement as the number of diffusion steps increases. Memory consumption does not grow significantly with additional steps; however, both inference and training time increase proportionally due to the reversible fusion design, where more steps naturally require additional computation.

In addition, our model supports images of various resolutions. As shown in Table 5, when testing with higher-resolution inputs (2x), we observe slight decreases in EI, AG, and SF, while $Q^{AB/F}$ and VIFF improve. The improvement in $Q^{AB/F}$ and VIFF can be attributed to the preservation of more fine-grained modality-specific details at higher resolutions, whereas the minor reductions in the other metrics may result from gradient dispersion introduced by increased spatial resolution. Although memory usage remains nearly unchanged, inference time increases substantially because the attention mechanism in the SD network has computational complexity that scales quadratically with image resolution.

8.11. Limitations and Broader Impacts

Although the proposed RED model achieves superior performance compared to existing methods and demonstrates strong generalization across diverse scenarios and tasks, several potential limitations remain. We introduce a reversible fusion paradigm that significantly reduces memory usage, enabling end-to-end training of diffusion models without relying on Markov chains and thereby avoid-

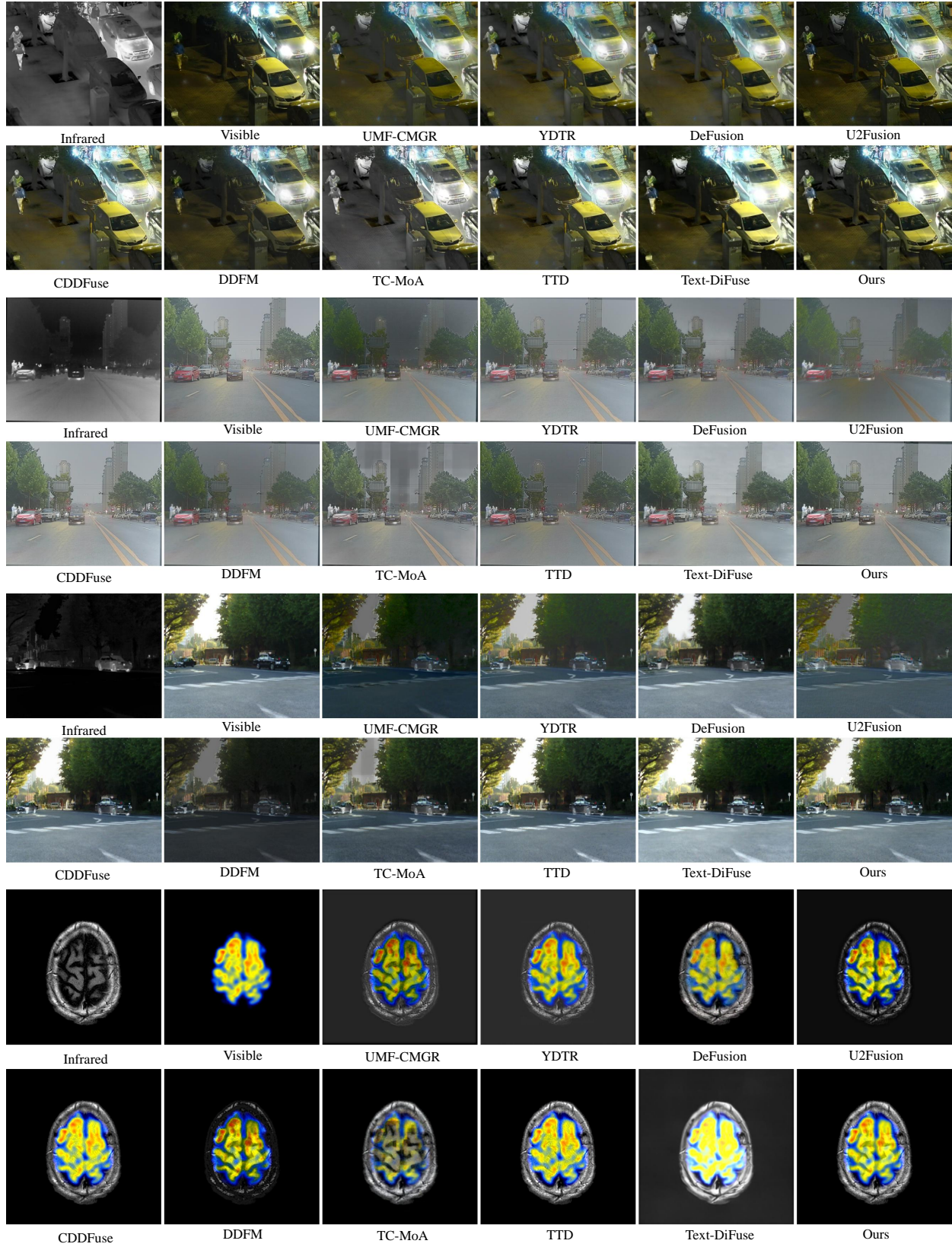


Figure 10. Visualization comparing SOTA methods.

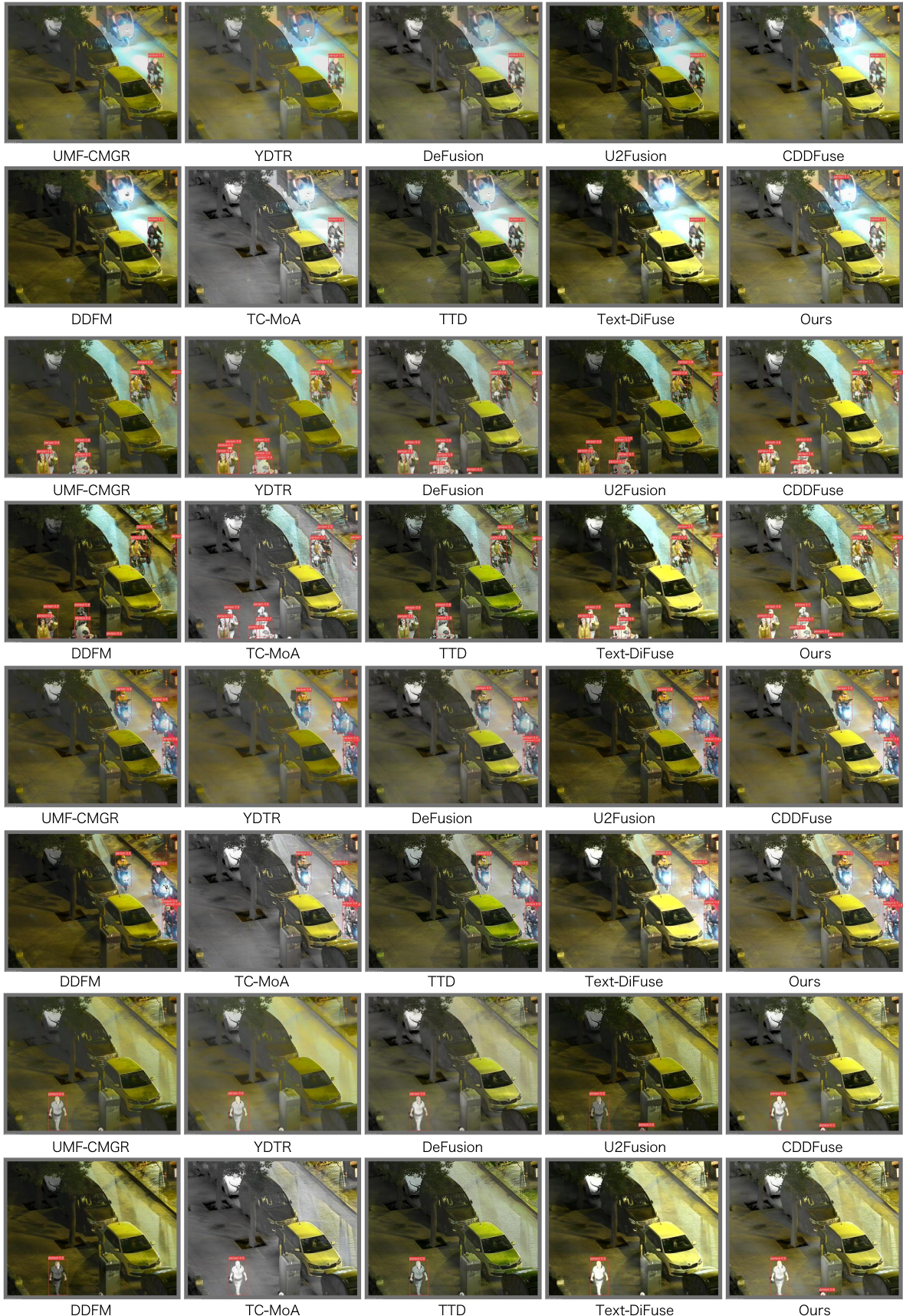


Figure 11. Visualization comparing SOTA methods on the object detection task.

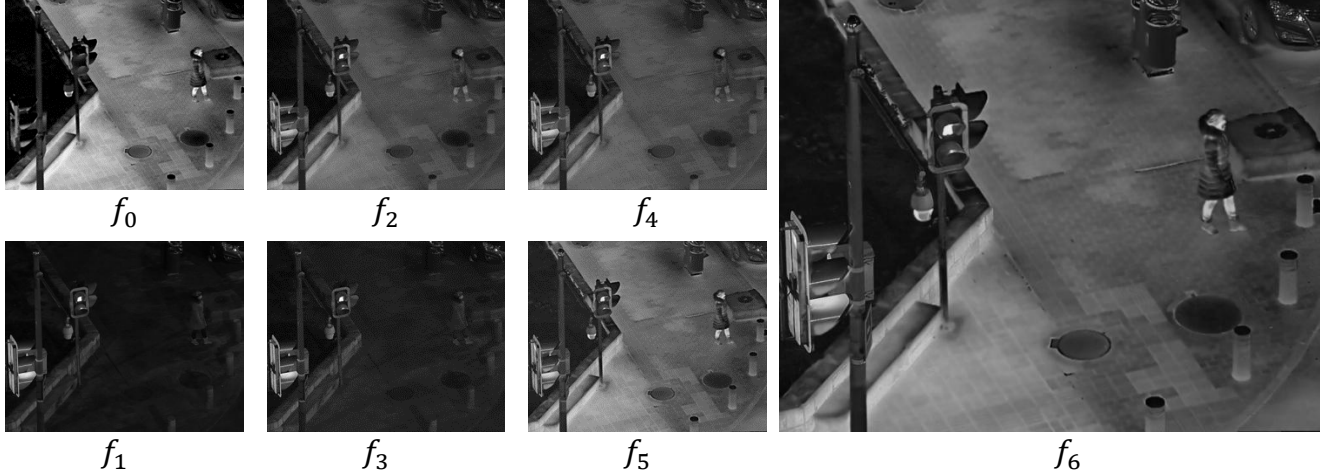


Figure 12. Visualization of Intermediate outputs during the inference at the diffusion step 6.

ing error accumulation that often leads to detail distortion. However, this memory-saving approach adopts a time-for-space trade-off, which results in slower training times. Additionally, the choice of the number of diffusion steps is currently empirical. While we observe that increasing the number of steps generally improves performance, an optimal step count cannot be precisely determined and may vary across tasks. From a broader societal perspective, the inability to guarantee an optimal trade-off between computational cost and performance could pose risks in high-stakes applications such as medical imaging and autonomous driving, where reliability and efficiency are critical.

References

- [1] Sumukh K Aithal, Pratyush Maini, Zachary Lipton, and J Zico Kolter. Understanding hallucinations in diffusion models through mode interpolation. *Advances in Neural Information Processing Systems*, 37:134614–134644, 2024. [7](#)
- [2] Lynton Ardizzone, Jakob Kruse, Sebastian Wirkert, Daniel Rahner, Eric W Pellegrini, Ralf S Klessen, Lena Maier-Hein, Carsten Rother, and Ullrich Köthe. Analyzing inverse problems with invertible neural networks. *arXiv preprint arXiv:1808.04730*, 2018. [3](#)
- [3] Jens Behrmann, Will Grathwohl, Ricky TQ Chen, David Duvenaud, and Jörn-Henrik Jacobsen. Invertible residual networks. In *International conference on machine learning*, pages 573–582. PMLR, 2019. [2](#)
- [4] Bing Cao, Yinan Xia, Yi Ding, Changqing Zhang, and Qinghua Hu. Test-time dynamic image fusion. *arXiv preprint arXiv:2411.02840*, 2024. [5, 7](#)
- [5] Bin Chen, Zhenyu Zhang, Weiqi Li, Chen Zhao, Jiwen Yu, Shijie Zhao, Jie Chen, and Jian Zhang. Invertible diffusion models for compressed sensing. *IEEE Transactions on Pattern Analysis and Machine Intelligence*, 2025. [3, 4](#)
- [6] Laurent Dinh, David Krueger, and Yoshua Bengio. Nice: Non-linear independent components estimation. *arXiv preprint arXiv:1410.8516*, 2014. [2](#)
- [7] Martin Genzel, Jan Macdonald, and Maximilian März. Solving inverse problems with deep neural networks—robustness included? *IEEE transactions on pattern analysis and machine intelligence*, 45(1):1119–1134, 2022. [3](#)
- [8] Aidan N Gomez, Mengye Ren, Raquel Urtasun, and Roger B Grosse. The reversible residual network: Backpropagation without storing activations. *Advances in neural information processing systems*, 30, 2017. [2, 3, 4](#)
- [9] Albert Gu and Tri Dao. Mamba: Linear-time sequence modeling with selective state spaces. *arXiv preprint arXiv:2312.00752*, 2023. [2](#)
- [10] Jonathan Ho, Ajay Jain, and Pieter Abbeel. Denoising diffusion probabilistic models. *Advances in neural information processing systems*, 33:6840–6851, 2020. [1, 2, 3](#)
- [11] Xinyu Jia, Chuang Zhu, Minzhen Li, Wenqi Tang, and Wenli Zhou. Llvip: A visible-infrared paired dataset for low-light vision. In *Proceedings of the IEEE/CVF international conference on computer vision*, pages 3496–3504, 2021. [4, 2](#)
- [12] Keith A. Johnson and J. Alex Becker. Harvard medical website, 2023. [4](#)
- [13] Rahima Khanam and Muhammad Hussain. Yolov11: An overview of the key architectural enhancements. *arXiv preprint arXiv:2410.17725*, 2024. [7](#)
- [14] Hui Li and Xiao-Jun Wu. Densefuse: A fusion approach to infrared and visible images. *IEEE Transactions on Image Processing*, 28(5):2614–2623, 2018. [2](#)
- [15] Hui Li, Xiao-Jun Wu, and Josef Kittler. Rfn-nest: An end-to-end residual fusion network for infrared and visible images. *Information Fusion*, 73:72–86, 2021. [2](#)
- [16] Zhe Li, Haiwei Pan, Kejia Zhang, Yuhua Wang, and Fengming Yu. Mambadfuse: A mamba-based dual-phase model for multi-modality image fusion. *arXiv preprint arXiv:2404.08406*, 2024. [2](#)
- [17] Pengwei Liang, Junjun Jiang, Xianming Liu, and Jiayi Ma. Fusion from decomposition: A self-supervised decomposition approach for image fusion. In *European Conference on Computer Vision*, pages 719–735. Springer, 2022. [5, 7](#)
- [18] Jinyuan Liu, Xin Fan, Zhanbo Huang, Guanyao Wu, Risheng Liu, Wei Zhong, and Zhongxuan Luo. Target-aware dual

adversarial learning and a multi-scenario multi-modality benchmark to fuse infrared and visible for object detection. In *Proceedings of the IEEE/CVF Conference on Computer Vision and Pattern Recognition*, pages 5802–5811, 2022. 4, 2

[19] Jiayi Ma, Linfeng Tang, Fan Fan, Jun Huang, Xiaoguang Mei, and Yong Ma. Swinfusion: Cross-domain long-range learning for general image fusion via swin transformer. *IEEE/CAA Journal of Automatica Sinica*, 9(7):1200–1217, 2022. 2

[20] Kangfu Mei, Nithin Gopalakrishnan Nai, and Vishal M Patel. Improving conditional diffusion models through re-noising from unconditional diffusion priors. In *2025 IEEE/CVF Winter Conference on Applications of Computer Vision (WACV)*, pages 3792–3801. IEEE, 2025. 7

[21] Alexander Quinn Nichol and Prafulla Dhariwal. Improved denoising diffusion probabilistic models. In *International conference on machine learning*, pages 8162–8171. PMLR, 2021. 2, 3

[22] Siran Peng, Xiangyu Zhu, Haoyu Deng, Liang-Jian Deng, and Zhen Lei. Fusionmamba: Efficient remote sensing image fusion with state space model. *IEEE Transactions on Geoscience and Remote Sensing*, 2024. 2

[23] K Ram Prabhakar, V Sai Srikanth, and R Venkatesh Babu. Deepfuse: A deep unsupervised approach for exposure fusion with extreme exposure image pairs. In *Proceedings of the IEEE international conference on computer vision*, pages 4714–4722, 2017. 2

[24] Robin Rombach, Andreas Blattmann, Dominik Lorenz, Patrick Esser, and Björn Ommer. High-resolution image synthesis with latent diffusion models. In *Proceedings of the IEEE/CVF conference on computer vision and pattern recognition*, pages 10684–10695, 2022. 1, 2

[25] Olaf Ronneberger, Philipp Fischer, and Thomas Brox. U-net: Convolutional networks for biomedical image segmentation. In *Medical image computing and computer-assisted intervention–MICCAI 2015: 18th international conference, Munich, Germany, October 5–9, 2015, proceedings, part III* 18, pages 234–241. Springer, 2015. 4

[26] Nataniel Ruiz, Yuanzhen Li, Varun Jampani, Yael Pritch, Michael Rubinstein, and Kfir Aberman. Dreambooth: Fine tuning text-to-image diffusion models for subject-driven generation. In *Proceedings of the IEEE/CVF conference on computer vision and pattern recognition*, pages 22500–22510, 2023. 1

[27] Jiaming Song, Chenlin Meng, and Stefano Ermon. Denoising diffusion implicit models. *arXiv preprint arXiv:2010.02502*, 2020. 2, 3

[28] Linfeng Tang, Jiteng Yuan, Hao Zhang, Xingyu Jiang, and Jiayi Ma. Piafusion: A progressive infrared and visible image fusion network based on illumination aware. *Information Fusion*, 83:79–92, 2022. 4, 2

[29] Wei Tang, Fazhi He, and Yu Liu. Ydtr: Infrared and visible image fusion via y-shape dynamic transformer. *IEEE Transactions on Multimedia*, 2022. 5, 7

[30] Bin Xu Wang and John J. Vastola. Diffusion models generate images like painters: an analytical theory of outline first, details later. *arXiv preprint arXiv:2303.02490*, 2023. 2

[31] Di Wang, Jinyuan Liu, Xin Fan, and Risheng Liu. Unsupervised misaligned infrared and visible image fusion via cross-modality image generation and registration. *arXiv preprint arXiv:2205.11876*, 2022. 5, 7

[32] Zhishe Wang, Yanlin Chen, Wenyu Shao, Hui Li, and Lei Zhang. Swinfuse: A residual swin transformer fusion network for infrared and visible images. *IEEE Transactions on Instrumentation and Measurement*, 71:1–12, 2022. 2

[33] Xinyu Xie, Yawen Cui, Tao Tan, Xubin Zheng, and Zitong Yu. Fusionmamba: Dynamic feature enhancement for multi-modal image fusion with mamba. *Visual Intelligence*, 2(1):37, 2024. 2

[34] Han Xu, Jiayi Ma, Junjun Jiang, Xiaojie Guo, and Haibin Ling. U2fusion: A unified unsupervised image fusion network. *IEEE Transactions on Pattern Analysis and Machine Intelligence*, 44(1):502–518, 2020. 5, 7

[35] Yu Yuan, Jiaqi Wu, Zhongliang Jing, Henry Leung, and Han Pan. Multimodal image fusion based on hybrid cnn-transformer and non-local cross-modal attention. *arXiv preprint arXiv:2210.09847*, 2022. 2

[36] Hao Zhang and Jiayi Ma. Sdnet: A versatile squeeze-and-decomposition network for real-time image fusion. *International Journal of Computer Vision*, 129:2761–2785, 2021. 2

[37] Hao Zhang, Lei Cao, and Jiayi Ma. Text-difuse: An interactive multi-modal image fusion framework based on text-modulated diffusion model. *arXiv preprint arXiv:2410.23905*, 2024. 5, 7, 8

[38] Yu Zhang, Yu Liu, Peng Sun, Han Yan, Xiaolin Zhao, and Li Zhang. Ifcnn: A general image fusion framework based on convolutional neural network. *Information Fusion*, 54:99–118, 2020. 2

[39] Chen Zhao, Shuming Liu, Karttikeya Mangalam, and Bernard Ghanem. Re2tal: Rewiring pretrained video backbones for reversible temporal action localization. In *Proceedings of the IEEE/CVF conference on computer vision and pattern recognition*, pages 10637–10647, 2023. 2, 3

[40] Zixiang Zhao, Haowen Bai, Jiangshe Zhang, Yulun Zhang, Shuang Xu, Zudi Lin, Radu Timofte, and Luc Van Gool. Cddfuse: Correlation-driven dual-branch feature decomposition for multi-modality image fusion. In *Proceedings of the IEEE/CVF conference on computer vision and pattern recognition*, pages 5906–5916, 2023. 2, 5, 7

[41] Zixiang Zhao, Haowen Bai, Yuanzhi Zhu, Jiangshe Zhang, Shuang Xu, Yulun Zhang, Kai Zhang, Deyu Meng, Radu Timofte, and Luc Van Gool. Ddfm: denoising diffusion model for multi-modality image fusion. *arXiv preprint arXiv:2303.06840*, 2023. 5, 7

[42] Pengfei Zhu, Yang Sun, Bing Cao, and Qinghua Hu. Task-customized mixture of adapters for general image fusion. *arXiv preprint arXiv:2403.12494*, 2024. 4, 5, 7